

A hybrid level-set-phase-field method for two-phase flow with contact lines

Martin Kronbichler* Gunilla Kreiss*

Abstract

We present a hybrid method combining a level set model with a phase field model. Contact line dynamics are represented by the full phase field model, whereas the convective interface transport and the evaluation of surface tension in the bulk of the domain are realized by a conservative level set model. This combination avoids the singularity at the contact line that is present in classical level set models with no-slip boundary conditions. The hybrid method relies on the similar shape of the concentration variable in the phase field model and the level set function. The terms specific to the phase field model are disabled away from the contact region by using a switch function. The benefits of using the level set model instead of the phase field model in the bulk of the domain are quantified by two extensive numerical benchmark computations. The conservative level set method gives considerably higher accuracy at the same mesh size than the phase field method. For the phase field method, a range of interface thicknesses and the mobilities are considered. The best values of these parameters for the two test cases are used in the comparison. Further, the well-posedness and stability of the hybrid method are shown using an a priori energy estimate. Numerical simulation of channel flow with the hybrid method demonstrates the increase in computational efficiency compared to a plain phase field model.

Key words. Contact line dynamics, phase field method, level set method, benchmark computation.

1 Introduction

The simulation of multi-phase flow with moving contact lines is of great practical importance in a wide range of applications, for instance for ink-jet printers, the prediction of subsurface flow and biomedical applications. However, the modeling of contact line dynamics requires special numerical treatment. The no-slip boundary condition that is used at solids for single-phase flow breaks down in the vicinity of contact lines, as shear stresses become singular [24]. It has been demonstrated that the singularity can be avoided if slip is allowed at the contact line [12, 23]. However, imposing slip velocities is delicate because a numerically feasible slip parameter can not easily be determined in experiments [11]. An additional modeling step is required

*Division of Scientific Computing, Department of Information Technology, Uppsala University, Box 337, 751 05 Uppsala, Sweden (martin.kronbichler@it.uu.se, gunilla.kreiss@it.uu.se).

when wetting forces influenced by the alignment of the interface with the solid need to be represented. Wetting phenomena arise in case the interface alignment with the solid deviates from the equilibrium position, the so-called static contact angle.

Several techniques have been proposed for numerically handling this setting. For example, the magnitude of slip has been proposed to depend on the apparent contact angle [49]. Alternatively, interface diffusion has been proposed as a tool for imposing contact angles and allowing the contact line to move in boundary integral [35], volume-of-fluid [45], and level set [55] simulations, respectively. Common to these approaches is an ad-hoc inclusion of the wetting mechanism, steered by some numerical parameters. Approaches for imposing contact line dynamics in a more physical way can be based on diffuse interface models, so-called phase field methods [26, 53]. These methods come with a built-in mechanism for contact line dynamics through a boundary condition on the underlying partial differential equations. However, diffuse interface models have higher numerical costs than other interface representation techniques like the level set method, the volume-of-fluid method, or surface tracking schemes. Also, the phase field method is often used for simulation of flows where the diffuse interface thickness and intermolecular mobility do not correspond to the underlying physics, but are rather numerically dictated by the available grid resolution. The behavior of discrete approximations with respect to the sharp-interface limit has been analyzed in [54]. Other approaches to contact line dynamics are multiscale methods. One variant is to combine a standard continuum model on the macroscopic scale with molecular dynamics simulations in order to represent mass diffusion over the interface around the contact line [41, 43, 44]. In another recently proposed multiscale model [32], the phase field model is used on the micro scale. This micro simulation determines an effective slip velocity, which is used as a boundary condition in the macro model.

In this work, we propose a hybrid method that combines the computational efficiency of the level set method with the contact line features of a phase field method. A hybrid approach combining level set and phase field features has been proposed previously [29], where the focus was to combine continuous surface tension models [8] popular in the level set community with the interface evolution of the phase field model. In the present work, the focus is instead on the region close to boundaries where the phase field model is a well-established approach for contact line dynamics. In regions away from the boundary, the complex processes for the interface evolution in the phase field method are both unnecessary and give rise to modeling errors due to the intermolecular mixing. We therefore disable the phase field interface diffusion away from the interface by using a switch function. Instead, we employ a conservative level set model with similar form of the interface profile [37] in the bulk region. We also provide a convergence study of the level set and phase field approaches when combined with the same flow solvers. This comparison quantifies the benefits from the combination of the two models in our hybrid approach.

The outline of this article is as follows. In Sec. 2, we present the two-phase flow models this work is based upon, the level set model and the phase field model. The numerical discretization is outlined in Sec. 3. In Sec. 4, we perform an in-depth convergence study of bubble dynamics for the two models on benchmark problems, the rise of a bubble due to gravity as well as the oscillations of a bubble due to surface tension. Sec. 5 presents the realization of the hybrid method, including a stability ar-

gument. Sec. 6 shows a numerical test of the hybrid method and concluding remarks are given in Sec. 7.

2 Multiphase flow models

We consider two-phase flow of immiscible incompressible fluids in a connected computational domain $\Omega \subset \mathbb{R}^d$ (spatial dimension $d = 2$ or 3). The governing equations are the *incompressible Navier–Stokes equations*

$$\rho \left(\frac{\partial \mathbf{u}}{\partial t} + \mathbf{u} \cdot \nabla \mathbf{u} \right) - \nabla \cdot (2\mu \nabla^s \mathbf{u}) + \nabla p = \mathbf{f}, \quad (1)$$

$$\nabla \cdot \mathbf{u} = 0. \quad (2)$$

The vector \mathbf{u} denotes the fluid velocity and p denotes the fluid’s (dynamic) pressure. The rate of deformation tensor is denoted by $\nabla^s \mathbf{u} = \frac{1}{2} (\nabla \mathbf{u} + (\nabla \mathbf{u})^T)$, the fluid density by ρ , and the fluid (dynamic) viscosity by μ . We denote by Ω_i the region occupied by fluid i with material parameters ρ_i and μ_i , and by Γ the free surface between the fluids. So-called jump conditions describe the relation of variables over the interface (see e.g. [13]),

$$\begin{aligned} \llbracket \mathbf{u} \rrbracket_{\Gamma} &= \mathbf{0}, \\ \llbracket -2\mu \varepsilon(\mathbf{u}) \cdot \mathbf{n} + p \mathbf{n} \rrbracket_{\Gamma} &= \sigma \kappa \cdot \mathbf{n}, \\ \llbracket -2\mu \varepsilon(\mathbf{u}) \cdot \mathbf{n} \rrbracket_{\Gamma} \cdot \mathbf{t} &= 0. \end{aligned}$$

Here, σ is the surface tension coefficient, \mathbf{n} denotes the unit normal on the interface pointing into fluid 1, and κ denotes the curvature. The notation $\llbracket \mathbf{u} \rrbracket = \mathbf{u}_1 - \mathbf{u}_2$ denotes the jump of quantities from one fluid to the other. In this work, we replace the explicit evaluation of jump conditions by posing the problem on the whole domain Ω and introducing surface tension as a volume force of the form

$$\mathbf{f}_{\text{st}} = \sigma \kappa \mathbf{n} \delta_{\Gamma}, \quad (3)$$

see, e.g., [39]. Here, δ_{Γ} is a delta function the localizes the force to the interface. Other body forces like gravity complement the forcing \mathbf{f} in the momentum equation. The Navier–Stokes system is closed by a divergence-free initial velocity field and suitable boundary conditions.

We also need to represent the interface, model its evolution, and specify how to implement the surface tension. In this paper we consider two models, the conservative level set model and the phase field model.

2.1 Conservative level set model

The conservative level set model, introduced in [37, 38], relies on a smoothed color function c instead of the signed distance function used in other level-set-based approaches as the ones described in [40, 51, 47, 39]. We assume a color function that takes the value -1 in the first fluid and $+1$ in the second one. The interface transport is expressed by an advection equation,

$$\frac{\partial c}{\partial t} + \mathbf{u} \cdot \nabla c = 0. \quad (4)$$

Due to the incompressibility condition (2), the interface transport can be equivalently be written as a conservation law. The shape of the interface profile is controlled by a reinitialization equation of the form

$$\frac{\partial c}{\partial \tau} + \nabla \cdot (\mathbf{n}(1 - c^2)) - \nabla \cdot (\mathbf{n}\varepsilon(\nabla c \cdot \mathbf{n})) = 0, \quad (5)$$

where τ is an artificial time and $\varepsilon \sim h$ controls the interface thickness. The reinitialization process involves solving the reinitialization equation (5) to steady state, where a balance between a compressive flux (second term) and diffusive flux (third term) normal to the interface is reached. For a plane interface normal to the x -direction, the interface profile is given by

$$c(x) = \tanh\left(\frac{x}{\varepsilon}\right). \quad (6)$$

We model the interface force by a continuous interface approach [8] based on the smoothed color function c ,

$$\mathbf{f}_{\text{st}} = \sigma \kappa \nabla H_\varepsilon(c), \quad (7)$$

where the curvature is computed from $\kappa = -\nabla \cdot \mathbf{n} = -\nabla \cdot (\nabla c / |\nabla c|)$ and H_ε denotes a discrete Heaviside function. The gradient of the Heaviside ∇H_ε approximates $\mathbf{n} \cdot \delta_{\Gamma}$ and has been demonstrated to give balanced forces when the finite element function spaces match [56]. Throughout this work, we use $(c + 1)/2$ as an approximation of the Heaviside. For this method, convergence to a sharp interface representation is expected as the interface thickness $\varepsilon = h$ approaches zero.

We note that the models for interface evolution and reinitialization are conservation laws, for which volume conservation is straight-forward, as opposed to standard level set methods where additional measures need to be taken, see, e.g., [50, 22, 28]. This simplicity comes at the price of higher resolution requirements when extracting curvature information from the steep profile around the interface.

2.2 Phase field model

Diffuse interface methods are based on the van der Waals hypothesis [52] that immiscible fluids actually mix on a molecular level. The concentration order parameter c of the phase field is defined by a balance of random molecular motion and molecular attraction, expressed by the molecular free energy density

$$f(c) = \beta_1 \Psi(c) + \frac{\beta_2}{2} |\nabla c|^2, \quad (8)$$

which is a sum of the bulk energy $\beta_1 \Psi(c)$ and the gradient energy $\frac{\beta_2}{2} |\nabla c|^2$. In this article, we assume a double well potential $\Psi(c) = \frac{1}{4}(c + 1)^2(c - 1)^2$ (see [26, 36] for different formulations of the bulk energy). The double well potential represents the separation into two stable states at $c = \pm 1$, balanced by the gradient that enforces a smooth transition. The system seeks to minimize the energy (8). The energy minimization over time is mathematically expressed by taking the variational derivative of the free energy $\int f d\Omega$ with respect to c and requiring conservation of the mass

fractions in the individual fluids. This gives the Cahn–Hilliard equation [9],

$$\frac{\partial c}{\partial t} = \nabla \cdot (m \nabla \phi), \quad (9)$$

$$\phi = \beta_1 \Psi'(c) - \beta_2 \nabla^2 c, \quad (10)$$

where ϕ denotes the chemical potential and the mobility factor is given by m . Different forms of the mobility, including a dependence on c , have been proposed, cf. [36], but we assume it to be constant in this work. The phase field method has been proposed for simulation of two-phase flow, e.g., in [2, 26, 27], see also [15, 48]. In the coupled Navier–Stokes/Cahn–Hilliard model, convective transport of the interface is included by adding the term $\mathbf{u} \cdot \nabla c$ to the left hand side in (9).

The surface tension along the interface according to (3) can be approximated by

$$\sigma \kappa \mathbf{n} \delta_\Gamma = \phi \nabla c, \quad (11)$$

which is of similar form as the one used for the continuous surface tension (7). We refer to [27, 7] for a comparative discussion of different forms for the interfacial force and [1] for a benchmark comparison. The strength of surface tension is encoded by the parameters β_1, β_2 . For a plain interface in x direction, it is given by

$$\sigma = \beta_2 \int_{-\infty}^{\infty} \left(\frac{\partial c}{\partial x} \right)^2 dx = \sqrt{\beta_1 \beta_2} \frac{2\sqrt{2}}{3},$$

where the equilibrium interface profile for a plane interface is

$$c(x) = \tanh \left(\sqrt{\frac{\beta_1}{2\beta_2}} x \right).$$

In order to effectively use the similar shape of the phase field concentration variable and the color function used in the level set formulation, we reformulate the Cahn–Hilliard equation by introducing the interface width ε and the surface tension σ . To this end, define $\beta_1 = 3\sigma/2\varepsilon$ and $\beta_2 = 3\sigma\varepsilon/4$, which gives the diffuse interface evolution equation

$$\frac{\partial c}{\partial t} + \mathbf{u} \cdot \nabla c - m \nabla^2 \phi = 0, \quad (12)$$

$$\phi - \frac{3\sigma\varepsilon}{4} \left(\frac{2}{\varepsilon^2} (c^3 - c) - \nabla^2 c \right) = 0. \quad (13)$$

In a non-dimensional form of (12)–(13), the Cahn number quantifies the interface width ε through $Cn = \varepsilon/L_c$ and the Péclet number gives an expression of the mobility, $Pe = L_c U_c \varepsilon / (m\sigma)$, using for a reference length L_c and reference velocity U_c , as used, e.g., in [53]. Note that the diffusion length $S = \sqrt{m\bar{\mu}}/L_c$ has been proposed as an alternative non-dimensional number for mobility [54].

Treatment of contact line dynamics. Consider the alignment of the interface at the boundary, which in static case is given by the static contact angle θ_0 , see Fig. 1. The

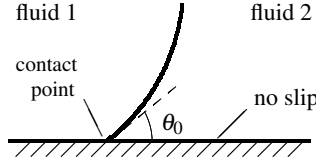


Figure 1: Static contact line with the static contact angle θ_0 .

phase field model can represent this setting through its boundary conditions, which are derived from a free surface energy (see [26, 53]),

$$\begin{aligned} \mathbf{n} \cdot \nabla c + \sigma \cos(\theta_0) g'(c) &= 0, \\ \mathbf{n} \cdot \nabla \phi &= 0, \end{aligned} \quad (14)$$

where $g'(c) = 1 - c^2$. We refer to [10] for a more general condition that includes hysteresis effects. The vector \mathbf{n} denotes the unit outer normal on the boundary. The built-in mechanism for moving contact lines in the phase field method and the related experimental work for finding appropriate material parameters is the main motivation for the hybrid method proposed in this work.

Convergence of the phase field model. For the phase field method (12)–(13), the parameters ε and m have a physical meaning as diffuse mixing lengths. Nonetheless, the method is designed as a tool for two-phase flow in the sharp interface limit $\varepsilon \rightarrow 0$ and $m \rightarrow 0$, see, e.g., the work by Jacqmin [26, Secs. 3, 4] and Lowengrub & Truskinovsky [33, Sec. 5]. The surface tension coefficient σ is the only parameter that is associated with a macroscopic value and retained in the limit. From a physical point of view, both ε and m are length scales of the order of magnitude of some tens of nanometers [11]. These values are often several orders of magnitude smaller than the size of the simulation domain and beyond the available numerical resolution. For this reason, the question of accuracy of the phase field model for finite values of ε and m with respect to the limit behavior has gained considerable attention. The work by Jacqmin [26] used an asymptotic analysis to relate the decay of m as $\varepsilon \rightarrow 0$ of the form

$$m = \mathcal{O}(\varepsilon^\delta). \quad (15)$$

Many numerical studies have been performed to evaluate this limit behavior, see, e.g., [33, 26, 53, 54] and references therein. The recent study [54] demonstrated convergence as $\varepsilon \rightarrow 0$ for fixed m for contact-line driven flow, i.e., $\delta = 0$ in (15). That study also identified an upper bound on the non-dimensional Cahn number Cn for getting converged results, which was found to be $Cn < 4S$, with $S = \sqrt{\mu m}/L$ the diffusion length scale, in the examples considered in [54].

When interpreting ε and m as numerical parameters perturbing the sharp interface limit, their value is usually set according to the available resolution. Previous works have used fixed relations of the form $\varepsilon = ch$ [1] or $\varepsilon = ch^\gamma$, where $\gamma \leq 1$ is chosen depending on the convergence rate of the numerical scheme [26]. In this article, we numerically determine the value of these quantities which give best accuracy. Since we are interested in the best possible accuracy for bubble dynamics, i.e., for flow that

is not in contact with solids, we include this test in the convergence study in Sec. 4.1.2 and Sec. 4.2.2 below.

3 Discretization

For time discretization, an implicit BDF-2 scheme [21] is employed, using a backward Euler step for the first time step when only one previous solution value is available. In order to avoid a nonlinear iteration due to the coupling of velocity and concentration, an explicit segregation approach is taken. For advancing from time level t^n to t^{n+1} , the velocity \mathbf{u} is first extrapolated to the new time level by the formula $\mathbf{u}^{n+1,*} = 2\mathbf{u}^n - \mathbf{u}^{n-1}$ (assuming a constant time step size). Then, the transport equation (4) or (12)–(13) is propagated to time t^{n+1} . The new values for c^{n+1} and ψ^{n+1} are eventually used in the propagation of the Navier–Stokes system. Note that this approach introduces a capillary time step limit for the level set implementation, see [18] for discussion.

For spatial discretization, we use the finite element method, which is implemented using routines of the deal.II library [3, 4]. For efficient evaluation of finite element operators, we use the approach presented in [30]. The domain Ω is subdivided into quadrilateral/brick elements of size h . Our implementation allows for adaptive mesh refinement, which is used to improve the resolution around the interface in several of the test cases considered below. We use the same mesh for both the flow variables and the level set/phase field variables.

3.1 The level set equation

For discretization of the level set advection (4) and reinitialization, (bi-)linear \mathcal{Q}_1 elements are chosen. Let us denote by $(\cdot, \cdot)_\Omega$ the standard L_2 inner product on the domain Ω . The discrete version of (4) is to find, at each time step, an approximation $c^{h,n+1}$ such that

$$\left(v_c^h, \frac{1}{2\Delta t} \left(3c^{h,n+1} - 4c^{h,n} + c^{h,n-1} \right) + \mathbf{u}^{n+1,*} \cdot \nabla c^{h,n+1} \right)_\Omega = 0 \quad (16)$$

holds for all discrete test functions $v_c^h \in V_c^h \subset H^1(\Omega)$, defined by (bi-)linear polynomials within elements and continuity over element boundaries. The resulting linear system is dominated by the mass matrix for small to moderate time steps and solved with a generalized minimum residual (GMRES) method [46]. All linear systems in this article are solved to a discrete l_2 residual of 10^{-9} .

In each time step, a fixed number of pseudo time steps of the reinitialization equation (5) is performed. Typically, three steps of size $\min(\Delta t, 0.3h)$ are used to retain a uniform shape of the color function c throughout the simulation. The interface thickness in the reinitialization is chosen to be $\varepsilon = h$ in all the examples with the level set method. The discretization is done with diffusion treated implicitly and convective compression explicitly. The normal \mathbf{n} is computed by first projecting $\nabla c^{h,n+1}$ on the discrete space given \mathcal{Q}_1^d elements,

$$\left(\mathbf{v}_n^h, \hat{\mathbf{n}}^h \right)_\Omega + \left(\nabla \mathbf{v}_n^h, \eta_n \hat{\mathbf{n}}^h \right)_\Omega = \left(\mathbf{v}_n^h, \nabla c^{h,n+1} \right)_\Omega, \quad (17)$$

which has to hold for all test functions on the finite element space associated to the normal. In this equation, $\eta_{\mathbf{n}} = 4h^2$ is a small diffusion to damp high frequency oscillations in the normal [56]. From the projected and filtered gradient, the filtered normal is computed by point-wise scaling $\mathbf{n}^h = \hat{\mathbf{n}}^h / |\hat{\mathbf{n}}^h|$. Based on the normal after reinitialization, we finally evaluate the curvature $\kappa^h = -\nabla \cdot \mathbf{n}^h$, using a filtering with diffusion $\eta_{\kappa} = \frac{1}{2}h^2$. The linear systems are solved with the conjugate gradient (CG) method [46].

3.2 The Cahn–Hilliard equation

In order to solve the Cahn–Hilliard equation (12)–(13) with standard bilinear \mathcal{Q}_1 finite elements which are only H^1 -conforming, the equation is discretized as a system and solved for $c^{h,n+1}, \phi^{h,n+1}$ in each time step.

We consider two variants for treating the nonlinear term $(c^{n+1})^3$ in the equation for the chemical potential (13). The first variant is a fully implicit BDF-2 discretization of the Cahn–Hilliard system with a Newton iteration to resolve the nonlinearity. The second variant is to treat the convective term explicitly by extrapolation and approximate the nonlinear potential term by a linearly stabilized splitting scheme as proposed in [16].

In the context of the BDF-2 scheme where two old solution values are available, the approximation introduced by the linearly stabilized scheme reads

$$(c^3 - c)^{(n+1)} \approx 2(c^3 - 3c)^{(n)} - (c^3 - 3c)^{(n-1)} + 2c^{(n+1)}. \quad (18)$$

The idea of the linearly stabilized scheme is to dominate the non-convex part in the double-well potential $\frac{1}{4}(c+1)^2(c-1)^2$ by the convex function c^2 , based on the interpretation of the Cahn–Hilliard equation as a gradient system. Likewise, the non-linearity in the boundary term (14) is approximated by the linearly stabilized splitting scheme

$$(1 - c^2)^{(n+1)} \approx 2(1 + 2s_{\theta}c - c^2)^{(n)} - (1 + 2s_{\theta}c - c^2)^{(n-1)} + 2s_{\theta}c^{(n+1)},$$

where $s_{\theta} = \text{sign}(\cos(\theta_0))$.

After introducing the finite element approximation similar to the one for the level set part, we obtain a 2×2 block matrix system

$$\begin{pmatrix} M & (2\Delta t/3)mK \\ -(3\sigma/\varepsilon)M - (3\sigma\varepsilon/4)K & M \end{pmatrix} \begin{pmatrix} C^{n+1} \\ \Phi^{n+1} \end{pmatrix} = \begin{pmatrix} F_c \\ F_{\phi} \end{pmatrix}, \quad (19)$$

where M denotes a mass matrix and K a Laplace matrix. The discrete solution values are denoted by C^{n+1} and Φ^{n+1} . This system is solved with GMRES using the block preconditioner proposed in [6]. The application of this preconditioner only requires vector operations and two evaluations of the inverse of the matrix $M + \sqrt{\sigma\varepsilon m\Delta t}/2K$. The inverse of this matrix is approximated by one V-cycle of the algebraic multilevel approach ML-AMG [19]. With this preconditioner, GMRES converges in 5–10 iterations for the problems considered in this article. The constant coefficient matrices in the linearly stabilized approach (together with an optimal linear solver) make the evolution of the phase field part comparably efficient, despite the fourth order spatial derivatives and the nonlinear double well potential.

In the fully implicit approach, a convective matrix $(2\Delta t/3)C(\mathbf{u}^{n+1,*})$ is added in the upper left block of the matrix and the matrix M in the lower left matrix is replaced by a potential matrix $J(c)$ that represents the double-well term. The evaluation of these matrices slightly increases numerical costs. However, larger time steps are possible with the fully implicit approach compared to the linearly stabilized scheme, as demonstrated in Fig. 8 below. Nonetheless, the same preconditioner as for the linearly stabilized case can be used for the fully implicit approach. Unless stated otherwise, the computational results with the phase field method are obtained with the linearly stabilized scheme.

3.3 Flow solver

In order to evaluate the interface representation accuracy of the level set model and the phase field model, we discretize the equations of incompressible flow with the same scheme for both models. We use the inf-sup stable element $\mathcal{Q}_2^d \mathcal{Q}_1$, i.e., biquadratic elements for each component of the velocity and bilinear elements for the pressure [14]. A fully implicit coupled discretization for the flow variables is chosen where the convective term is discretized in skew-symmetric form [42]. The nonlinear convection terms are resolved in a Newton iteration which usually takes 1–2 iterations to converge. The resulting saddle point linear system is solved with GMRES preconditioned by a Schur-complement based block triangular preconditioner. The Schur complement is approximated by a scheme based on the underlying time-dependent Stokes operator [34, 5]. This gives convergence in 5–25 iterations when using an incomplete LU decomposition for the velocity block and an ML-AMG [19] V-cycle on the pressure Laplacian.

4 Accuracy of level set and phase field methods

In this section, we evaluate the performance of the phase field model compared to the level set model. For both models, the flow solver dominates the computational costs when efficient linear solvers for the level set and phase field variables are used. Hence, the accuracy on a given mesh size is a good indication of the numerical efficiency of the respective numerical method. We also note in our simulations that the computing time of the phase field part and the level set part in the two models are very similar. This illustrates the efficiency of the iterative solver presented in Sec. 3.2, which makes the costs for the more complicated Cahn–Hilliard system comparable to the level set evolution and the curvature evaluation. We collect results for two test cases, a rising bubble test according to the benchmark defined in [25] in Sec. 4.1 and an oscillating bubble in Sec. 4.2.

4.1 Rising bubble test

We consider one of the rising bubble tests proposed in [25] and recently evaluated for the phase field method in [1]. A bubble of light fluid of diameter $d_0 = 0.5$ is surrounded by a heavier fluid (density contrast $\rho_1/\rho_2 = 10$) and rises due to gravitational forces. The motion gives rise to a deformation of the bubble shape. The

domain size	d_0	ρ_1	ρ_2	μ_1	μ_2	g	σ	Re	Eo
1×2	0.5	1000	100	10	1	0.98	24.5	35	10

Table 1: Parameters for the rising bubble test [25].

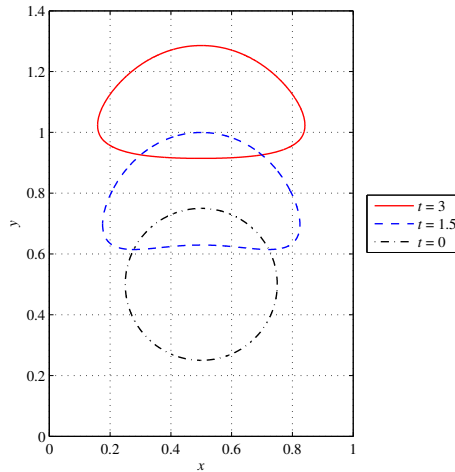


Figure 2: Schematic view of the domain for the rising bubble test [25] with bubble location at times 0, 1.5, and 3.

parameters for the benchmark test are summarized in Table 1, with subscript 1 denoting material properties of the outside fluid and subscript 2 those of the bubble. The fluid is characterized by a Reynolds number $\text{Re} = \rho_1 U_g d_0 / \mu_1 = 35$ and Eötvös number $\text{Eo} = \rho_1 U_g^2 d_0 / \sigma = 10$, where the gravitational velocity is denoted by $U_g = \sqrt{g d_0}$. For this choice of the parameters, surface tension forces are strong, which makes this benchmark suited for evaluating the behavior of phase field and the level set models for flows with medium to high surface tension effects.

Symmetry boundary conditions are set on the left and right boundaries at $\{x = 0\}$ and $\{x = 1\}$, and no-slip velocity boundary conditions on the lower and upper boundaries. Since the fluid pressure is only determined up to a constant, it is fixed to 0 in the lower left corner of the domain. For the level set and phase field part, no-flux conditions are used all over the domain boundary. The simulation is run until time $t = 3$.

As in [25], we record three scalar quantities in each time step,

- the degree of circularity of the bubble,

$$c = \frac{\text{perimeter of area-equivalent circle}}{\text{perimeter of bubble}} = \frac{\sqrt{\pi A_B}}{P_B}, \quad (20)$$

where P_B denotes the perimeter of the bubble and A_B the area of the bubble (compare with Fig. 3(a)),

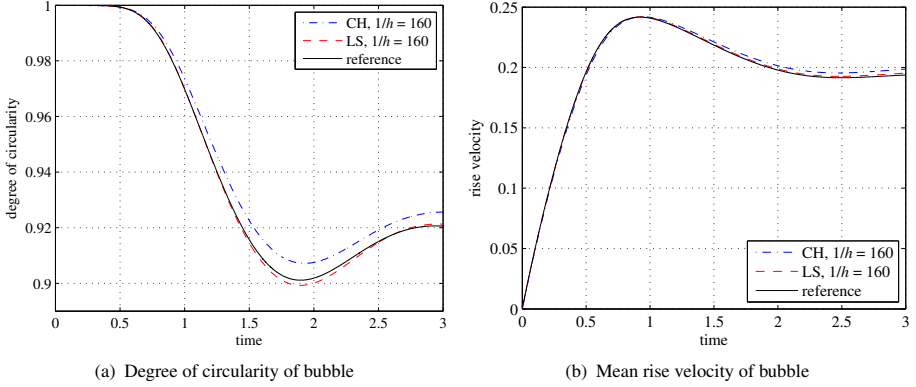


Figure 3: Quantities considered in the rising bubble test. The graphs include numerical results at $h = 1/160$ for the conservative level set model (LS), see Sec. 2.1, and the phase field model (CH), see Sec. 2.2.

- the mean rise velocity of the bubble,

$$V_B = \frac{\int_{\Omega_1} u_2 d\mathbf{x}}{\int_{\Omega_1} d\mathbf{x}}, \quad (21)$$

where Ω_1 is the region occupied by the bubble (compare with Fig. 3(b)), and

- the location of the center of mass of the bubble,

$$y_c = \frac{\int_{\Omega_1} x_2 d\mathbf{x}}{\int_{\Omega_1} d\mathbf{x}}. \quad (22)$$

The region Ω_1 is defined as the fraction of the domain where $c > 0$ for both models. In our implementation, this domain is computed by finding zeros of the linear finite element interpolants on element edges.

Our evaluation compares the prediction of the benchmark quantities at a certain resolution level to a numerically computed reference solution. The reference solution has been obtained on a fine mesh solution with the conservative level set method, using a mesh size $h = 1/2560$ around the interface and $h = 1/320$ away from the interface, and with time step $\Delta t = 0.00025$. The reference solution is based on a grid that is two or more levels finer than the quantities that are compared against it. We found that this yields better error approximations and more realistic convergence rates than if the refinement level was only required to differ by one (as, e.g., in [25]). We evaluate relative discrete errors in time $\|e\|_p = \|q - q_{\text{ref}}\|_p / \|q_{\text{ref}}\|_p$ for $p = 1, 2, \infty$ for the three benchmark quantities. Moreover, estimated rates of convergence (ROC) and extreme values of the benchmark quantities are reported.

4.1.1 Results for the level set method

Table 2 shows the number of degrees of freedom (velocity, pressure, level set variable), the number of time steps, and computing times used at different mesh sizes for

$1/h$	NDOF	NTS	CPU
40	18,000	200	22
80	42,000	375	109
160	96,000	750	450
320	240,000	1,500	2,600
640	680,000	3,000	10,000
1280	1,020,000	6,000	31,000
2560	1,750,000	12,000	110,000

Table 2: Number of degrees of freedom (NDOF) for all three variables (velocity, pressure, level set), number of time steps (NTS), and CPU time in seconds for the conservative level set method. Adaptive mesh refinement is used and average numbers of degrees of freedom are given.

$1/h$	c_{\min}	$t _{c_{\min}}$	$V_{B,\max}$	$t _{V_{B,\max}}$	$y_c(t=3)$
Ref. [25]	0.9012 ± 0.0001	1.90 ± 0.02	0.2419 ± 0.0002	0.925 ± 0.005	1.081 ± 0.001
40	0.7543	2.620	0.2456	0.970	1.0868
80	0.8931	1.926	0.2428	0.942	1.0825
160	0.8992	1.895	0.2420	0.930	1.0814
320	0.90046	1.901	0.24174	0.924	1.0813
640	0.90089	1.900	0.24168	0.924	1.08146
1280	0.90106	1.898	0.241663	0.923	1.08156
2560	0.90114	1.898	0.241660	0.921	1.08162

Table 3: Minimum circularity and maximum rise velocity, with corresponding time of incidence, and the final position of the center of mass for the level set method for the rising bubble benchmark [25]. The time step size is chosen to be $\Delta t = 0.64h$.

the level set method (similar to the data collected in [25]). The computing times are recorded on an Intel i7-2620M notebook processor at 2.7 GHz when running the program in serial. Note that the results in Fig. 8 suggest that the time step sizes could be increased without compromising accuracy, see Sec. 4.1.3 below. This would result in a reduction of computing times. Table 3 compares level set results at different mesh sizes for the minimum circularity over time, the maximum rise velocity and the center of mass at the final time $t = 3$, also including the highly resolved reference results.

Next we justify the use of adaptively refined meshes around the interface. Starting from a coarse mesh that represents the geometry, the mesh is hierarchically refined up to the finest level on which computations are performed. In order to concentrate the work to the representation of the interface, the mesh is adapted dynamically during the simulation. For a given fine mesh size h_{\min} associated with hierarchical level l_{\max} , we flag a cell K for coarsening if

$$\|c^2 - 1\|_{\infty,K} < 0.001 \cdot 10^{l_K - l_{\max}},$$

where l_K denotes the level of cell K , and mark a cell for refinement if the value has become larger than this threshold. This algorithm keeps a band of successively finer cells around the interface using the value of the level set function. In order to prevent cells from becoming too coarse, we do not allow coarsening when some maximal mesh size h_{\max} is exceeded. The deal.II library refinement and coarsening routines [3]

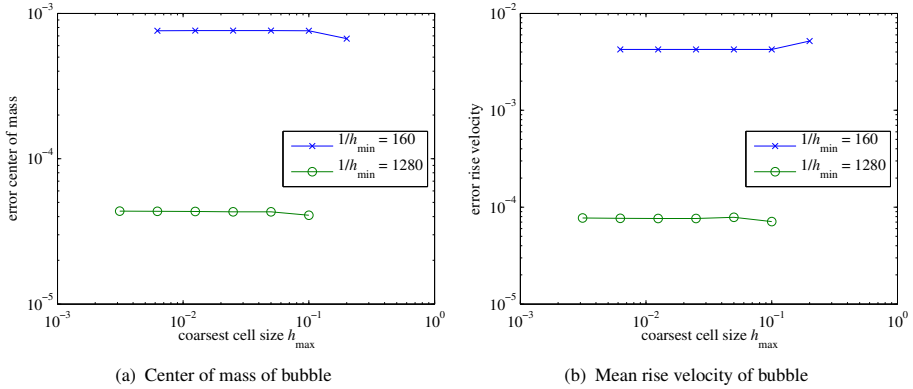


Figure 4: Error depending on the coarsest allowed mesh size in adaptive algorithm in level set method.

$1/h$	NDOF	NTS	CPU
40	36,000	500	36
80	140,000	750	210
160	570,000	1500	1,600
320	2,260,000	3,000	9,900
640	9,020,000	6,000	69,000

Table 4: Number of degrees of freedom (NDOF) for all four variables (velocity, pressure, concentration, chemical potential), number of time steps (NTS), and CPU time in seconds for the phase field model. Uniform meshes are used.

have a smoothing effect on the mesh. They ensure that two neighboring cells differ by at most one grid level, which can limit the coarsest cell size actually present in the simulation. In Fig. 4, we compare computations where we vary the coarsest allowed mesh size, using two different values of the finest mesh size h_{\min} . It can be seen that the results are insensitive to the mesh size in the far field. For the case $h = 1/160$, the results with coarse meshes in the far field have around 8,000 cells, whereas a homogeneously refined mesh at $h = 1/160$ has 51,200 cells. These results suggest that the given test case has very low resolution requirements in the far field.

4.1.2 Results for the phase field method

In Table 4, we summarize the number of time steps taken for the computations with the phase field model. The tests presented in this section are based on uniform meshes in order to exclude mesh effects when testing the accuracy for different values of the interface thickness ε and the mobility m . Therefore, the computing times for a given mesh size are larger compared to the ones for the conservative level set method in Table 2. However, we have also tested adaptive meshes with a refinement strategy based on gradient jumps over faces [17] for the concentration variable c . A similar strategy has been used in [1]. Similarly to the test with the conservative level set method in Fig. 4, we observed very little sensitivity of the accuracy on the mesh size away from the interface.

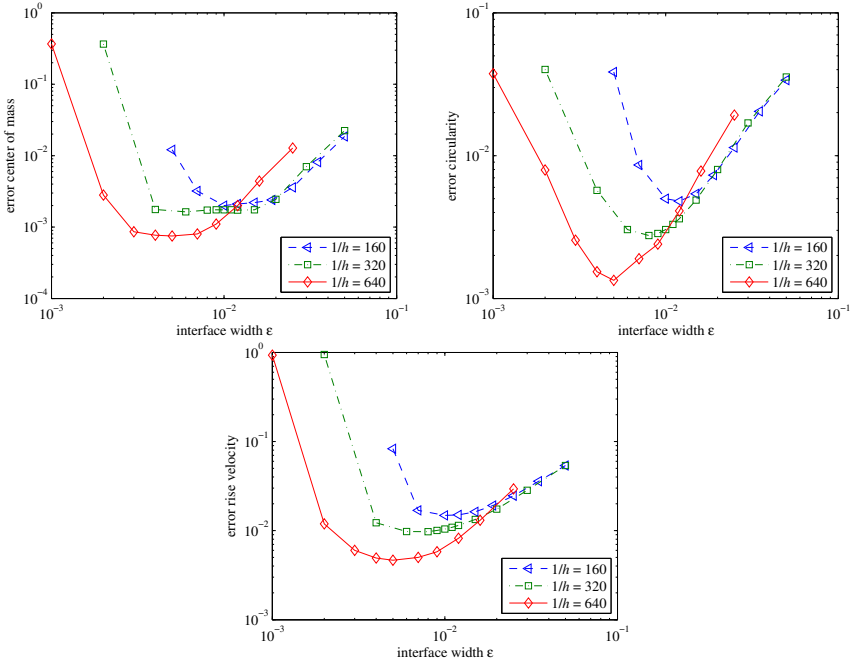


Figure 5: l_2 errors in time for the phase field method for three different mesh sizes at fixed mobility constant $m(h)$ (according to the best value found in Fig. 6) and varying diffuse interface width ϵ .

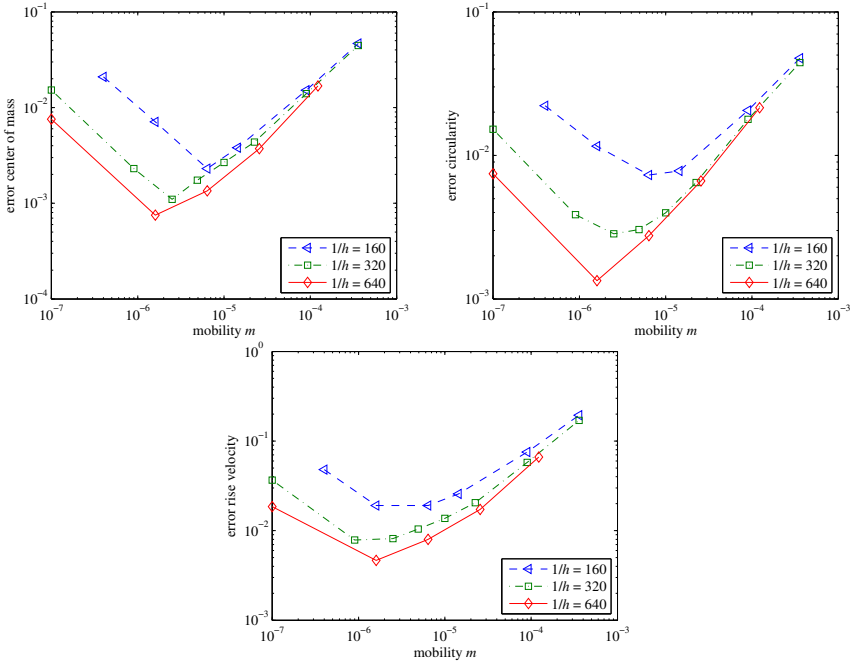


Figure 6: l_2 errors in time for the phase field method for three different mesh sizes at fixed diffuse interface width $\epsilon(h)$ (according to the best value found in Fig. 5) and varying mobility.

$1/h$	ε	m	c_{\min}	$t _{c_{\min}}$	$V_{B,\max}$	$t _{V_{B,\max}}$	$y_c(t=3)$
Ref. [25]			0.9012 ± 0.0001	1.90 ± 0.02	0.2419 ± 0.0002	0.925 ± 0.005	1.081 ± 0.001
40	$2h$	$2.2e-5$	0.9403	2.028	0.2415	1.068	1.0929
80	$2h$	$1.0e-5$	0.9159	1.921	0.2420	0.965	1.0892
160	$1.9h$	$6.4e-6$	0.9072	1.923	0.2420	0.942	1.0856
320	$2.6h$	$2.5e-6$	0.9048	1.912	0.2423	0.934	1.0851
640	$3.2h$	$1.6e-6$	0.9040	1.926	0.2411	0.931	1.0830

Table 5: Minimum circularity and maximum rise velocity with corresponding time of incidence, and the final position of the center of mass for the phase field method with parameters for ε and m that give best results for the rising bubble benchmark [25]. The time step size is chosen to be $\Delta t = 0.32h$.

In order to find the values that give best agreement with the reference solution, we run simulations for a range of parameters m and ε . For each mesh size, we find an optimal pair (ε, m) by varying one quantity at a time while keeping the other fixed. This process is performed in two iterations in order to account for the fact that the best value of ε is to be found for an optimal value of the mobility m . In the following, we only show the final results with the best values for the parameters.

Fig. 5 shows numerical errors for different values of the interface thickness ε at three different mesh sizes. On a given mesh, the mobility m is kept constant for all values of ε and chosen to the value which gives the smallest error. The values of the mobility m that have been used can be found in Table 5. It can be seen that the best results are obtained for an interface width ε between $2h$ and $3h$, which is somewhat smaller than the value $\varepsilon = 5h$ used in [1]. In Fig. 5, we can see that the quality of the solution is similar over a range of the interface thickness ε between $2h$ and $4h$. This suggests that for $\varepsilon < 4h$, the interface dynamics are not completely resolved. Nonetheless, a reduction of the diffuse interface width still has a beneficial effect on the accuracy as the perturbation of the sharp interface limit becomes smaller.

Fig. 6 shows the numerical error when the interface thickness ε is kept fixed and the mobility is varied. The interface thickness has been chosen to the value that gives the least error as reported in Table 5. The minimum error in the benchmark is obtained for values of the mobility between 10^{-5} and 10^{-6} , scaling approximately as h .

4.1.3 Convergence comparison

Let us now compare the accuracy provided by the conservative level set model and the phase field model for this test case. We also include the best results from the benchmark study [25], namely those obtained with the TP2D code, in our comparison.¹ We compare all results against the highly resolved level set computation with $h = 1/2560$ around the interface. Convergence rates with the level set model are linear for the center of mass and more than linear for the circularity and the rise velocity. Note that the large improvements in the level set results for circularity at coarse meshes are due to oscillations of the level set function c around the interface in regions where $\kappa \gtrsim 0.2/h$. For the phase field model, we observe linear speed of convergence on all benchmark quantities.

¹Downloaded on 5 November 2011 from http://www.featflow.de/en/benchmarks/cfdbenchmarking/bubble/bubble_reference.html

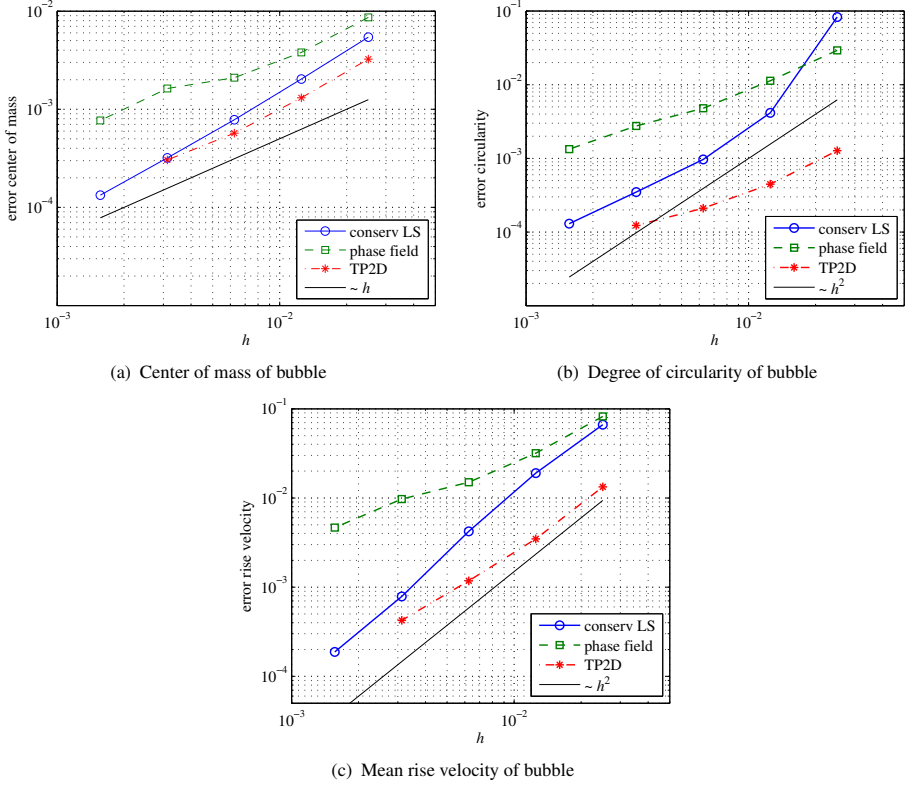


Figure 7: Convergence of discrete l_2 error in time of the conservative level set method, the phase field method, and the level set approach TP2D from [25, group 1].

Compared to the TP2D code which is based on a standard level set method, our method needs more than twice as much resolution for the circularity around the interface and almost twice as much resolution for the rise velocity and center of mass at most grid levels in the test. However, the conservative level set method shows a faster speed of convergence. The use of adaptivity in our implementation allows to concentrate the resolution to a region around the interface without compromising overall accuracy. In our computations, we allowed the mesh far away from the interface to be by up to a factor 8 coarser as the mesh around the interface. However, we would expect similar gains with the standard level set model as well.

Finally, we quantify the error made by the time stepping scheme for the two models in Fig. 8 by comparing different sizes of the time step Δt . Note that the time step size is restricted by a capillary limit due to the explicit treatment of surface tension for both methods [18]. The results show that the BDF-2 time discretization allows for relatively large time steps without notable effect on the accuracy. The same holds true for the phase field method when a fully implicit Newton approach is used. If instead the linearly stabilized scheme for the double-well potential (18) is employed, a substantial time error at larger step sizes is observed. However, one often uses small time steps for phase field implementations in the range $\Delta t < 0.1h/\|\mathbf{u}\|_\infty$, a case where the splitting error in this linearization is small.

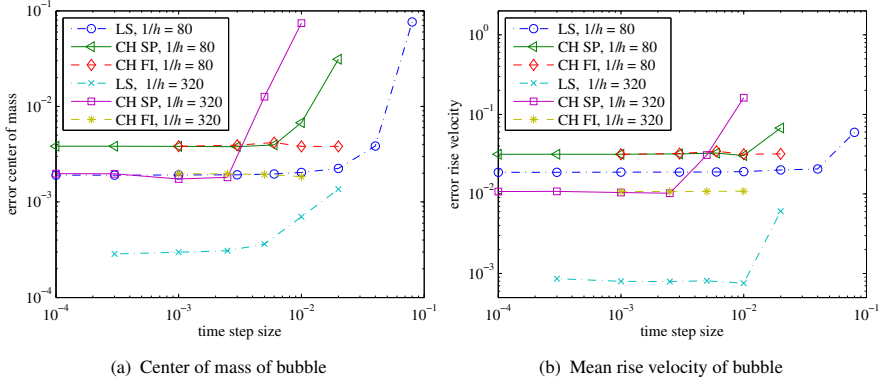


Figure 8: Error for two different mesh sizes in the conservative level set method (LS) and the phase field method (CH). For the phase field method, a linearly stabilized scheme according to (18) that treats convection and nonlinear term explicitly (CH SP) and a fully implicit BDF-2 time stepping with Newton iteration (CH FI) are compared.

When comparing the error between the two models, Fig. 8 shows that the conservative level set model remains stable for larger values of the time step. Also, the level set model gives more accurate results already for substantially larger values of the time step size compared to the phase field model. Hence, the possibility of larger time steps increases the efficiency gain with the level set model compared to the phase field model further.

4.2 Oscillating bubble

As a second test, we consider the relaxation of an ellipse to circular shape at zero gravity. As an initial condition, we choose an ellipse with main axes 0.75 and 0.3333, see Fig. 9. The computational domain is $[-2.5, 2.5]^2$ and the simulation is run to time $t = 2$. We choose $\rho = 1$ and $\mu = 0.1$ for both fluids. The surface tension coefficient is set to $\sigma = 10$. In this example, surface tension is the only active forcing, and the flow is characterized by the Ohnesorge number

$$\text{Oh} = \frac{\mu}{\sqrt{\rho\sigma L}} = 0.0316, \quad (23)$$

where $L = 1$ is the diameter of the circle with the same area as the initial ellipse. Compared to the rising bubble test which mainly stresses the interface representation and interaction between inertial forces and surface tension, this test case puts more emphasis on the interplay between viscous forces and surface tension.

Similarly to the rising bubble test, we consider two scalar quantities to determine the quality of the solutions,

- the mean velocity in x -direction of the right half of the bubble,

$$U_B = \frac{\int_{\Omega_1 \cap \{x > 0\}} u_1 \, d\mathbf{x}}{\int_{\Omega_1 \cap \{x > 0\}} d\mathbf{x}}, \quad (24)$$

compare with Fig. 10, and

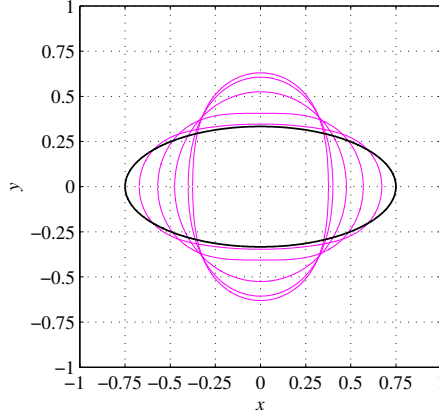


Figure 9: Configuration for the ellipsoidal bubble at the start of the simulation (thick line) and at times $t = 0.05, 0.1, 0.15, 0.2, 0.25$ (thin lines), i.e., until the first turning point.

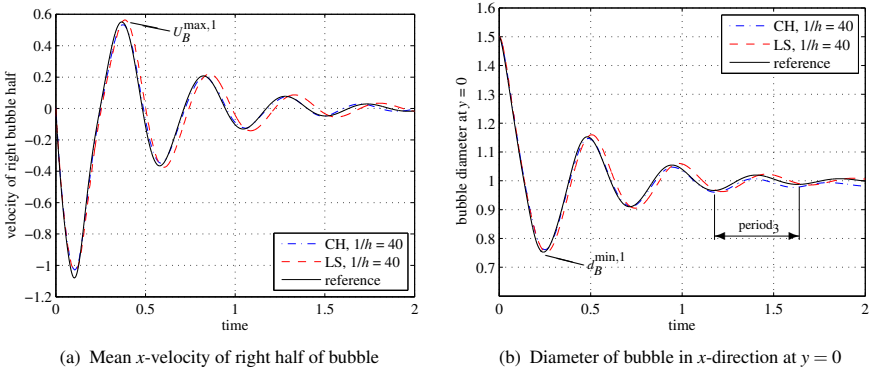


Figure 10: Time evolution of benchmark quantities for the oscillating bubble test case. The plots show a reference solution at a fine mesh and a phase field (CH) and level set (LS) result at $h = 1/40$, respectively.

- the diameter d_B of the bubble along the x -axis at $y = 0$.

The benchmark quantities are displayed in Fig. 10, including two numerical solutions at $h = 1/40$. As a reference result for evaluating errors, we again use a highly resolved level set result, this time with mesh resolution $h = 1/160$ away from the interface and $h = 1/640$ close to the interface.

4.2.1 Convergence comparison

For both methods, we first consider the accuracy of extremal point quantities on the oscillating bubble test case. We show the prediction of

- the first maximum of the mean velocity in the right half of the bubble $U_B^{\max,1}$,
- the first minimum in the diameter of the bubble along the line $\{y = 0\}$, $d_B^{\min,1}$, and
- the period between oscillations measured as the time between the third and the

$1/h$	$U_B^{\max,1}$	$t _{U_B^{\max,1}}$	$d_B^{\min,1}$	$t _{d_B^{\min,1}}$	period ₃
20	0.4941	0.430	0.7821	0.284	0.535
40	0.5641	0.386	0.7523	0.259	0.476
80	0.5617	0.373	0.7496	0.248	0.463
160	0.5549	0.3695	0.7514	0.2435	0.460
320	0.5524	0.3683	0.7522	0.2425	0.4588
640	0.5516	0.3678	0.7524	0.2423	0.4587

Table 6: Oscillating bubble with level set method. Value of velocity of right bubble half at first maximum, diameter of bubble at the first minimum point, and period between the third and fourth diameter minimum. Times of incidence are also given.

$1/h$	ε	m	$U_B^{\max,1}$	$t _{U_B^{\max,1}}$	$d_B^{\min,1}$	$t _{d_B^{\min,1}}$	period ₃
20	1.2h	2e-4	0.5142	0.369	0.7690	0.246	0.425
40	1.2h	1e-4	0.5331	0.377	0.7612	0.251	0.447
80	1.6h	5e-5	0.5418	0.372	0.7570	0.248	0.456
120	2.4h	3.3e-5	0.5471	0.368	0.7549	0.246	0.458

Table 7: Oscillating bubble with phase field method, using the best parameters for ε and m , cf. Figs. 12 and 13. Value of velocity of right bubble half at first maximum, diameter of bubble at the first minimum point, and period between the third and fourth diameter minimum. Times of incidence are also given.

fourth minimum of the bubble diameter at $\{y = 0\}$ (minima at times $t = 1.175$ and $t = 1.634$, respectively),

see also Fig. 10. Table 6 shows results with the conservative level set model and Table 7 shows the respective results with the phase field model. As for the rising bubble test case, we summarize the convergence behavior of the two methods by a plot with rates of convergence in Fig. 11. For this test case, the phase field method performs considerably better than the conservative level set method for coarse meshes. However, the level set method again converges more quickly as the mesh is refined, and it gives better results at finer meshes size. By comparing Tables 6 and 7, one can see that the level set method poorly predicts the period in the oscillations at coarse meshes. This indicates that the effect of surface tension force is not as accurately represented on coarse meshes compared to the phase field method.

4.2.2 Phase field parameters

As before, we test the sensitivity of the phase with respect to the interface thickness ε and mobility m . In Fig. 12, we display the error compared to the highly resolved level set reference solution when ε is varied. The mobility is kept constant in this test at the value that gives the smallest error, see the discussion in Sec. 4.1.2. In Fig. 13, we display the respective experiments when ε is kept fixed for a given mesh and the mobility m is varied. We observe best results when the interface thickness is chosen between $1.2h$ and $2.4h$ and when the mobility is proportional to h . Compared to the rising bubble test, the interface thicknesses ε that give best results are closer to h . This suggests that the diffuse interface representation is simpler in this case and can be represented accurately already for smaller values of ε/h .

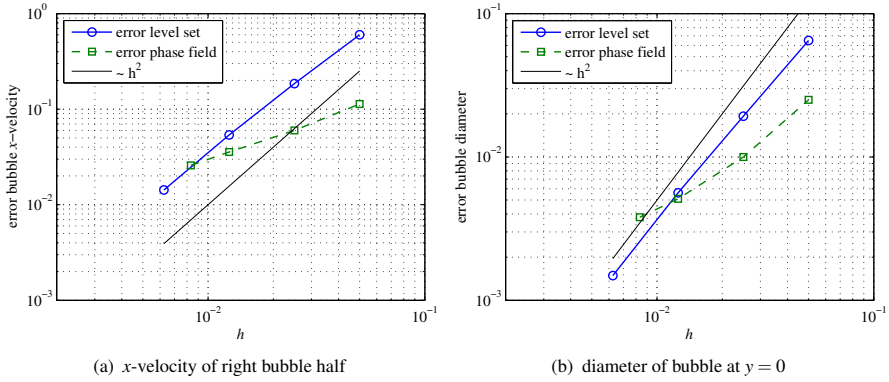


Figure 11: Convergence of discrete l_2 error in time of the conservative level set model and the phase field model on the oscillating ellipse test case.

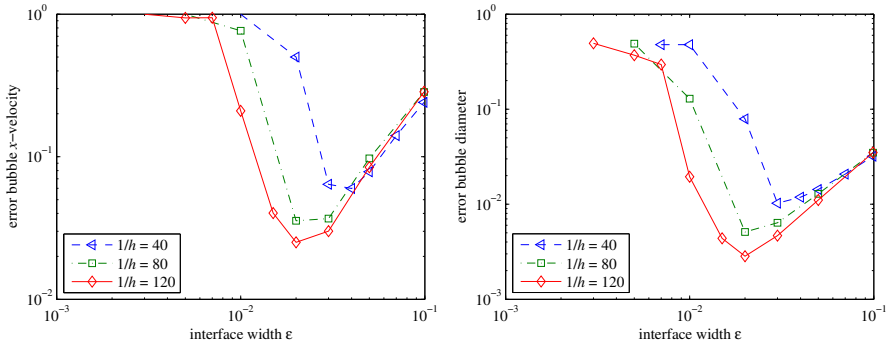


Figure 12: l_2 errors in time for oscillating bubble for three different mesh sizes at fixed mobility $m(h)$ (see Table 7) and varying diffuse interface width ϵ .

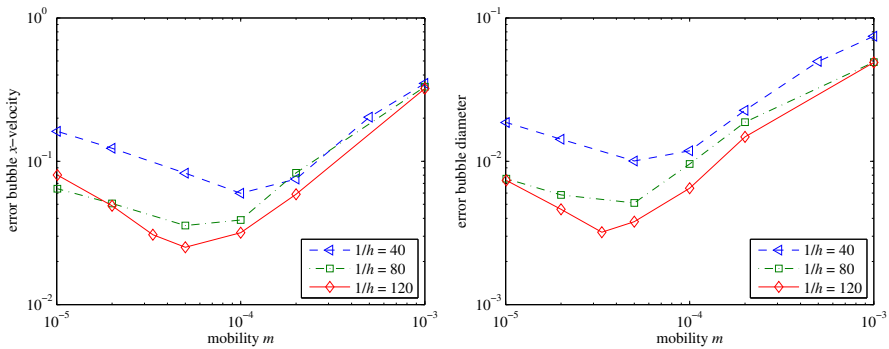


Figure 13: l_2 errors in time for oscillating bubble for three different mesh sizes at fixed diffuse interface width $\epsilon(h)$ (see Table 7) and varying mobility.

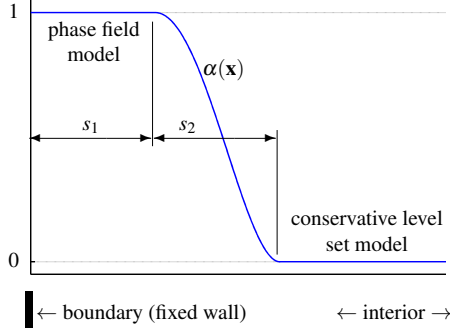


Figure 14: Schematic illustration of the switch function $\alpha(\mathbf{x})$ in one dimension.

5 Hybrid method

The two benchmark tests of bubble dynamics illustrate the superior convergence properties of the conservative level set method compared to the phase field method. In particular for the rising bubble test where external forces (gravity) are active, the level set method gives considerably better results than the phase field method. This observation suggests to construct a method that retains the level set method for representing the interface away from contact lines. However, we want to use the phase field method around the contact region in order to directly account for contact line dynamics, since the level set method combined with no-slip boundary conditions includes no mechanism for handling this setting [24]. The combination is realized by a switch function,

$$\alpha(\mathbf{x}) = r\left(\frac{s_1 - d_w(\mathbf{x})}{s_2}\right), \quad r(y) = \begin{cases} 1, & y \leq 0, \\ (y+1)^2(y-1)^2, & 0 < y < 1, \\ 0, & \text{else,} \end{cases} \quad (25)$$

where $d_w(\mathbf{x})$ denotes the closest distance from the point \mathbf{x} to a wall. The switch function α can be used to select between phase field terms and level set terms. A smooth transition ensures that the regularity of the solution is retained. The switch function is inspired from filtering functions proposed for hybrid RANS/LES modeling in turbulence research [20]. Fig. 14 gives an illustration of the switch function α in one spatial dimension. We note that $\alpha \in C^1(\Omega)$.

By using the switch function, we modify the evolution equation from the phase field model (12)–(13) to the following hybrid form:

$$\begin{aligned} \frac{\partial c}{\partial t} + \mathbf{u} \cdot \nabla c - \nabla \cdot (\alpha m \nabla \phi) &= 0, \\ \phi - \frac{3\sigma}{4\varepsilon} (2\Psi'(c) - \varepsilon^2 \nabla^2 c) &= 0. \end{aligned} \quad (26)$$

In regions away from the boundary, the switch function $\alpha = 0$ disables the diffuse interface transport and the plain level set advection equation is used. In regions close the contact point, however, the switch function $\alpha = 1$ gives the full phase field model.

In order to accurately capture the contact line dynamics, the phase field region needs to be chosen large enough. At the same time, we do not want to make it unnecessarily large in order to retain the efficiency of the level set model in the bulk of

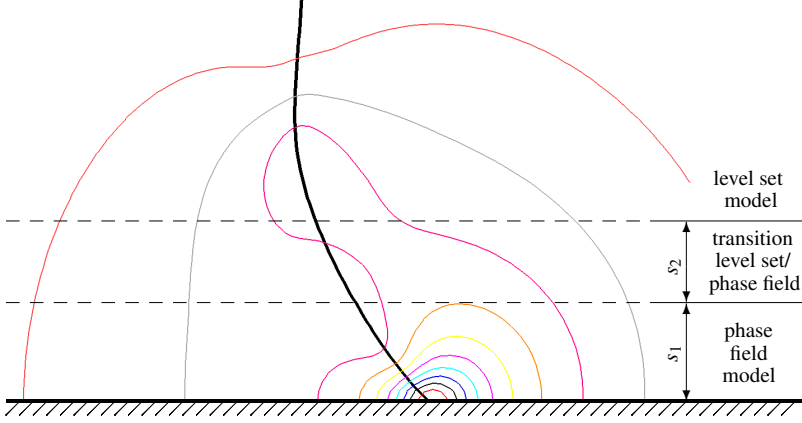


Figure 15: Representation of the phase field diffusive interface transport close to the contact line including the phase field region in the hybrid method. The thick line represents the position of the interface $\{c = 0\}$. Isocontour lines of the chemical potential are represented by thin lines.

the domain. The size of the region over which diffusive interface transport is relevant is proportional to $\sqrt{\mu m}$ as motivated in [54], see Fig. 15. Therefore, we choose $s_1 = 4\sqrt{\mu m}$ in our computations. In another region of size $s_2 = 2\sqrt{\mu m}$, we let the switch function α change from value one to zero. If the diffusion length is chosen proportional to the mesh size, this approach effectively limits the size of the phase field region.

In the hybrid approach presented in [29], the surface tension force is computed using the continuous surface tension form of the level set computations using the curvature $\kappa = -\nabla \cdot \mathbf{n}$. However, the full phase field method is used for the interface evolution. Compared to that approach, our hybrid method avoids the modeling perturbations of magnitudes $\mathcal{O}(\varepsilon) + \mathcal{O}(m)$ in regions away from the contact line. Instead, the error made by the conservative level set model compared to a sharp interface limit is purely numerical and decreasing quickly. According to the accuracy tests in Sec. 4, this gives considerably faster convergence than the phase field method, which promises higher accuracy than when using the phase field evolution everywhere.

In addition to the evolution of the interface, we also need to evaluate interfacial tension and reinitialize the level set function. We propose the following algorithm:

- (i) Advance the hybrid equation (26).
- (ii) Reinitialize level set equation using the modified reinitialization equation

$$\frac{\partial c}{\partial \tau} + \nabla \cdot (\mathbf{n}(1 - \alpha)(1 - c^2)) - \nabla \cdot (\mathbf{n}(1 - \alpha)\varepsilon \nabla c \cdot \mathbf{n}) = 0.$$

- (iii) Compute normal vectors $\mathbf{n} = \nabla c / |\nabla c|$ and curvature $\kappa = -\nabla \cdot \mathbf{n}$ using the filtered projection (17) in the whole domain.
- (iv) Evaluate the modified surface tension force in the momentum equation,

$$\mathbf{f}_{\text{st}} = (\alpha \phi + \sigma(1 - \alpha)\kappa)\nabla c.$$

- (v) Advance velocity and pressure through the Navier–Stokes equations.

5.1 Analysis of stability

In this section, we discuss the stability of the hybrid method. We assume the divergence-free velocity field \mathbf{u} to be given. In other words, we neglect the nonlinear coupling to the Navier–Stokes equations in the analysis presented in this section. The weak form of the Cahn–Hilliard equation with modified mobility is to find $c \in V_c = H^1(\Omega)$ and $\phi \in V_\phi = H^1(\Omega)$ such that

$$\left(v_c, \frac{\partial c}{\partial t} + \mathbf{u} \cdot \nabla c \right)_\Omega + (\nabla v_c, \alpha m \nabla \phi)_\Omega = 0, \quad (27)$$

$$(v_\phi, \phi - \beta_1 \Psi'(c))_\Omega - (\nabla v_\phi, \beta_2 \nabla c)_\Omega - (v_\phi, \beta_2 \cos(\theta_0)(1 - c^2))_{\Gamma_{\text{wall}}} = 0, \quad (28)$$

holds for all test functions $v_c \in V_c$ associated to the concentration variable c and all $v_\phi \in V_\phi$ associated to the chemical potential variable ϕ . The double well potential is given by $\Psi(c) = \frac{1}{4}(c-1)^2(c+1)^2$ as before. For simplicity of notation, we write the equation with parameters $\beta_1 = 3\sigma/2\varepsilon$ and $\beta_2 = 3\sigma\varepsilon/4$ as in Sec. 2.2 instead of σ and ε .

Proposition 1 (Continuous a priori energy estimate). *Assume $c, \phi \in H^2(\Omega)$, sufficient regularity on \mathbf{u} , and $\alpha(\mathbf{x}) \geq 0$. Further assume that $\cos(\theta_0) = 0$. We define the Cahn–Hilliard internal energy as*

$$\mathcal{F}(c) = \beta_1 \Psi(c(:,t)) + \frac{\beta_2}{2} |\nabla c(:,t)|^2.$$

Then, the solution to the system (27)–(28) satisfies the energy inequality

$$\mathcal{E}(c;t) := \int_\Omega \mathcal{F}(c(:,t)) d\mathbf{x} \leq \mathcal{E}(c;0) - \int_0^t \int_{\partial\Omega} \mathbf{u} \cdot \mathbf{n} \mathcal{F}(c(:,\tau)) ds d\tau, \quad (29)$$

where the last term on the right hand is the energy production due to inflow and the energy loss due to outflow.

Proof. We follow the concept of energy estimates for the Cahn–Hilliard equation written as a system, discussed, e.g., in [36]. Since the parameters β_1, β_2 are positive and the double-well potential is non-negative for all concentration functions c , it holds that $\mathcal{E}(c;t) \geq 0$ and hence the energy is well-defined.

At a given time instance t , we choose the particular test function $v_c = \phi(:,t)$ in (27). This gives

$$\left(\phi, \frac{\partial c}{\partial t} + \mathbf{u} \cdot \nabla c \right)_\Omega + (\nabla \phi, \alpha m \nabla \phi)_\Omega = 0. \quad (30)$$

Likewise, we choose the test function v_ϕ equal to $\frac{\partial c}{\partial t} + \mathbf{u} \cdot \nabla c$ in (28), yielding

$$\left(\frac{\partial c}{\partial t} + \mathbf{u} \cdot \nabla c, \phi - \beta_1 \Psi'(c) \right)_\Omega - \left(\frac{\partial}{\partial t} \nabla c + \nabla(\mathbf{u} \cdot \nabla c), \beta_2 \nabla c \right)_\Omega = 0. \quad (31)$$

We use the smoothness of c to rewrite $\Psi'(c) \frac{\partial c}{\partial t} = \frac{\partial}{\partial t} \Psi(c)$ and $\nabla c \frac{\partial}{\partial t} \nabla c = \frac{1}{2} \frac{\partial}{\partial t} |\nabla c|^2$. If we then subtract (31) from (30), we get

$$\begin{aligned} & (\nabla \phi, \alpha m \nabla \phi)_\Omega + \beta_1 \int_\Omega \frac{\partial}{\partial t} \Psi(c) d\mathbf{x} + \frac{\beta_2}{2} \int_\Omega \frac{\partial}{\partial t} |\nabla c|^2 d\mathbf{x} \\ & + (\mathbf{u} \cdot \nabla c, \beta_1 \Psi'(c))_\Omega + (\nabla(\mathbf{u} \cdot \nabla c), \beta_1 \nabla c)_\Omega = 0. \end{aligned}$$

Using the Gauss–Green theorem and that $\nabla \cdot \mathbf{u} = 0$, the terms on the second line can be simplified to

$$\begin{aligned} (\mathbf{u} \cdot \nabla c, \Psi'(c))_{\Omega} + (\nabla \cdot \mathbf{u}, \Psi'(c))_{\Omega} &= \int_{\Omega} \nabla \cdot (\mathbf{u} \Psi'(c)) d\mathbf{x} = \int_{\partial\Omega} \mathbf{u} \cdot \mathbf{n} \Psi'(c) ds, \\ (\nabla(\mathbf{u} \cdot \nabla c), \nabla c)_{\Omega} + \frac{1}{2} (\nabla \cdot \mathbf{u}, |\nabla c|^2)_{\Omega} &= \frac{1}{2} \int_{\Omega} \nabla \cdot (\mathbf{u} |\nabla c|^2) d\mathbf{x} = \frac{1}{2} \int_{\partial\Omega} \mathbf{u} \cdot \mathbf{n} |\nabla c|^2 ds, \end{aligned}$$

where \mathbf{n} denotes the unit outer normal on the boundaries. Hence, the energy in (29) satisfies the equality

$$(\nabla\phi, \alpha m \nabla\phi)_{\Omega} + \frac{\partial \mathcal{E}(c; t)}{\partial t} + (\mathbf{u} \cdot \mathbf{n}, \mathcal{F}(c))_{\partial\Omega} = 0. \quad (32)$$

The term $(\nabla\phi, \alpha m \nabla\phi)_{\Omega}$ is a dissipative term that is non-negative in Ω because $\alpha m \geq 0$ by construction of the switch function α . Hence, we have that

$$\frac{\partial}{\partial t} \mathcal{E}(c; t) \leq - \int_{\partial\Omega} \mathbf{u} \cdot \mathbf{n} \mathcal{F}(c(\cdot, \tau)) ds,$$

which shows the assertion. \square

Corollary 2. *Assume sufficiently smooth initial data and a sufficiently smooth switch function α . Then, the description of the coupled level-set-phase-field equation (27)–(28) is a well-posed system.*

Proof. For $\alpha(\mathbf{x}) \geq \alpha_0 > 0$, the problem is well-posed by the standard Cahn–Hilliard theory [36]. It remains to show that $\alpha(\mathbf{x}) \geq 0$ suffices for well-posedness.

Since $\mathcal{E}(c; t) \leq \mathcal{E}(c; 0)$, we know that $\|c\|_{H^1} \leq C$, where the constant C only depends on initial data and boundary data but not on α and the solution c . For sufficiently smooth initial data, it follows that higher derivatives $\|c\|_{H^k}$, $k \geq 1$, are bounded in a similar way. From the definition of the chemical potential (13), it follows that

$$\|\phi\|_{H^{k-1}} \leq C_k, \quad (33)$$

which shows that both c and ϕ as well as their derivatives are bounded by initial and boundary data, independently of α . We can construct a sequence of problems with $\alpha^n(\mathbf{x}) > 0$, where $\lim_{n \rightarrow \infty} \alpha^n(\mathbf{x}) = \alpha(\mathbf{x})$ satisfies the relaxed condition $\alpha(\mathbf{x}) \geq 0$. Since the corresponding solutions are bounded independently of α , the result follows by a compactness argument. \square

Remark 3. *Proposition 1 can be extended to the case with non-perpendicular contact angle, which yields an additional energy production term $\int_{\Gamma_{\text{wall}}} \beta_2 \cos(\theta_0) (c - \frac{1}{3}c^3) ds$.*

The result from Proposition 1 shows that the Cahn–Hilliard energy $\mathcal{E}(c)$ only increases because of inflow through boundaries where $\mathbf{u} \cdot \mathbf{n} < 0$ and possibly by contact line dynamics with non-perpendicular static contact angles according to Remark 3. There is no internally generated energy production due to the switch function α . Rather, the energy is decaying due to the Cahn–Hilliard diffusion in regions where $\alpha > 0$ and unchanged elsewhere.

In the discrete case, we enforce the weak form (27)–(28) in discrete admissible function spaces $V_*^h \subset H^1(\Omega)$. These discrete spaces are defined by \mathcal{L}_1 finite elements

on a given mesh. Below, we show stability of the function switch if we disregard the effect of fluid velocity. To account for fluid velocity is more challenging in the discrete case because the term $\frac{\partial c}{\partial t} + \mathbf{u} \cdot \nabla c$ is discontinuous over element boundaries for standard H^1 finite elements. Hence it is not in the function space V_ϕ^h , which is necessary for establishing equation (31). However, the realization of the switch function does not depend on velocity and hence, we disregard it in the stability proof.

Proposition 4. *Assume that $\mathbf{u} \equiv 0$ in (27) and $\cos(\theta_0) = 0$. Then, the numerical approximation to system (27)–(28) satisfies the energy inequality*

$$\mathcal{E}(c^h; t) := \int_{\Omega} \mathcal{F}(c^h) d\mathbf{x} \leq \mathcal{E}(c^h; 0), \quad (34)$$

and hence the discretization of the switch function is stable.

Proof. We proceed similarly as in the proof of Proposition 1. At a given time instance t , we choose the particular test function $\phi(\cdot, t) \in V_c^h$ in (27). This gives

$$\left(\phi, \frac{\partial c}{\partial t} \right)_{\Omega} + (\nabla \phi, \alpha m \nabla \phi)_{\Omega} = 0. \quad (35)$$

Likewise, we choose the test function v_ϕ equal to $\frac{\partial c}{\partial t} \in V_c^h$ in (28),

$$\left(\frac{\partial c}{\partial t}, \phi \right)_{\Omega} - \left(\frac{\partial c}{\partial t}, \beta_1 \Psi'(c) \right)_{\Omega} - \left(\frac{\partial}{\partial t} \nabla c, \beta_2 \nabla c \right)_{\Omega} = 0. \quad (36)$$

Subtracting (36) from (35), we get

$$(\nabla \phi, \alpha m \nabla \phi)_{\Omega} + \beta_1 \int_{\Omega} \frac{\partial}{\partial t} \Psi(c) d\mathbf{x} + \frac{\beta_2}{2} \int_{\Omega} \frac{\partial}{\partial t} |\nabla c|^2 d\mathbf{x} = 0.$$

Since $\alpha m \geq 0$ in Ω by construction of α , we have that

$$\frac{\partial}{\partial t} \mathcal{E}(c; t) = -(\nabla \phi, \alpha m \nabla \phi)_{\Omega} \leq 0,$$

which shows the assertion. \square

6 Numerical results with the hybrid method

For testing the hybrid approach, we consider two-phase flow in a channel, see Fig. 16. The computational domain consists of two cylindrical regions of diameter 1 and 2, respectively, which are connected by a conical part of length 1. We consider materials that correspond to oil for the first fluid and water for the second fluid, see Table 8. The flow is driven by inflow of water from the left boundary and, to a lesser extent, forces introduced by the contact line. The inflow velocity is given by a laminar profile of the form

$$u_1(\mathbf{x}, t) = \begin{cases} 4 \sin(\pi t)(0.5 - x_2)(0.5 + x_2), & 0 < t < 0.5, \\ 4(0.5 - x_2)(0.5 + x_2), & \text{else.} \end{cases}$$

The Reynolds number computed for material parameters of oil with unit length and unit velocity scale is equal to 10. The simulation starts with a straight interface located

ρ_1	ρ_2	μ_1	μ_2	σ	Re	θ_0
1000	1370	100	33	100	10	140°

Table 8: Parameters for channel flow.

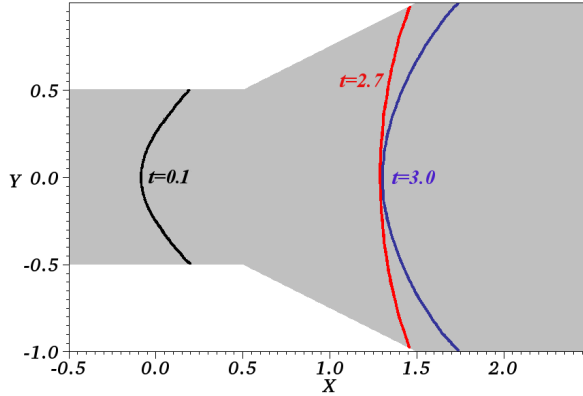


Figure 16: Computational domain with interface position at three different times.

at $x_1 = 0$. The imposed contact angle is 40 degrees, measured from the water side (i.e., water is wetting). In the simulation, this condition is imposed by setting $\cos(\theta_0) = -0.766$ where water corresponds to $c = 1$ and oil to $c = -1$. Since the static contact angle is different from the interface alignment of the initial condition, the interface quickly adopts a skew profile, as illustrated in Fig. 16 at $t = 0.1$. After the initial transient, the profile keeps its shape and moves with steady speed according to the inflow velocity until it reaches the sharp corner at $x_1 = 0.5$. Here, the interface changes shape in order to adopt to the different angle of the wall. The interface then continues moving with decreasing speed as the channel gets wider. At $x_1 = 1.5$, the second sharp corner requires a second change in the angle. We run the simulation until time $t = 4.5$ when the contact region is close to the right end of the channel at $x_1 = 2.5$.

In Fig. 17, we show results from computations using the phase field model in the whole domain at three different mesh sizes. We use a computational mesh that consists of square elements of length h for $x_1 \in (-0.5, 0.5)$ and extend the mesh through the conical part by using elements of trapezoidal shape. In the cylindrical part at the right, the resulting elements have aspect ratio 1 : 2 between x_1 and x_2 direction. As a time step size, we use $\Delta t = 0.1h$. We choose the phase field parameters to be $\varepsilon = 2h$ and $m = 10^{-4}h$. During the simulation, we record the location of the interface at the wall, defined as the point where $c = 0$. The irregularities as the interface moves over the corners at times $t_1 \approx 0.75$ and $t_2 \approx 2.7$ are distinctive features of this example. In particular when moving over the second corner, some oscillations of the interface develop due to inertial effects. The numerical errors introduced at these irregular points are relatively large, which is clearly visible in Fig. 17. We will use the solution on the finest mesh as reference solution.

In Fig. 18, we compare the results of the hybrid method with the phase field model at a mesh size $h = 0.025$. It can be seen that the hybrid solution is considerably closer to the reference solution. This is particularly evident from the detailed view

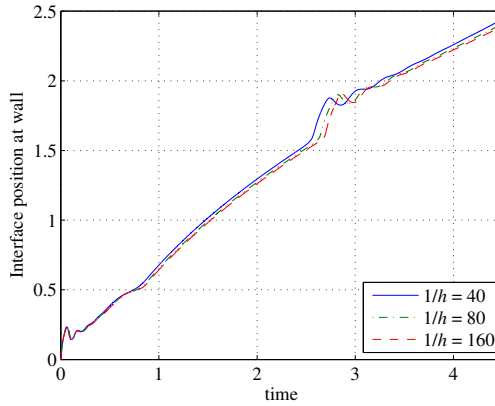


Figure 17: Location of the interface at the wall boundary as a function of time using the phase field method at three different resolutions.

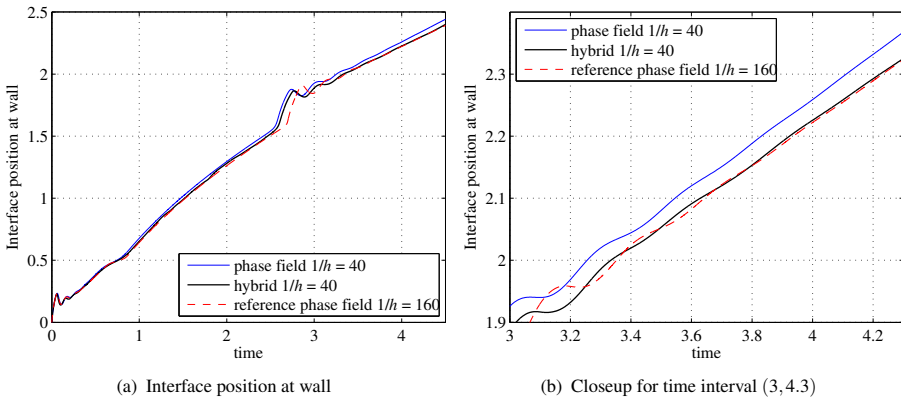


Figure 18: Comparison of the hybrid solution and the phase field solution at $h = 0.025$. As a reference result, we include phase field results at $h = 0.00625$. It can be seen that the hybrid solution is very close to the highly resolved phase field solution, compared to the global phase field solution.

in Fig. 18(b). The results show that for this example the hybrid method gives considerably better prediction of the accumulated effect of the interface motion along the wall.

Efficient implementations of the hybrid method can be devised by combining a relatively coarser mesh in the level set domain with higher resolution around the contact region. This way, the increased resolution requirements in the phase field method can be balanced with the requirements in the level set part, as demonstrated in [31].

7 Conclusions

We have presented a hybrid method for the simulation of incompressible immiscible two-phase flow where the interface is in contact with solid walls. The method combines a level set model in the interior of the domain with a phase field model close to contact lines. This combination is made possible by a specific choice of the level

set function as a smoothed color function that has a similar shape as the concentration parameter in the phase field method. Computational tests on channel flow with strong surface tension illustrate the beneficial properties of this combination, compared to using a phase field model all over the domain. This approach promises increased computational efficiency for problems where the phase field method alone is expensive because of excessive resolution requirements. In particular, we expect even better effects for three-dimensional simulations where mesh resolution is more limited.

The accuracy of the level set model and the phase field model for representing bubble dynamics, i.e., flow without contact lines, has been evaluated on two benchmark examples. We have performed simulations with both models using the same solver for the Navier–Stokes equations in order to specifically test interface representation and evolution as well as the evaluation of surface tension. We found the level set model to show better convergence speed and to give more accurate results for the same mesh size than the phase field model in many cases. We also evaluated the impact of the time step size on the accuracy of the two methods. The results indicate that large time steps are possible also for the phase field method, as long as a fully implicit Newton scheme is used. A linearly stabilized splitting approach gives a faster implementation but requires smaller time steps in order not to perturb the results. Moreover, a systematic study for finding the best size of the diffuse interface thickness and mobility for the test cases has been performed. Values of ε between $2h$ and $3h$ have been found to give a good compromise between accurate interface representation and small modeling errors due to the diffuse interface thickness.

The evaluation of the rising bubble benchmark test has also illustrated the improved accuracy of standard level set methods based on a signed distance functions from the work in [25]. Therefore, a hybrid method using signed distance functions for the level set part promises even better accuracy. However, such a formulation does not allow for straight-forward combination with the phase field function because the solution variables do not have a similar shape. One alternative would be to introduce the level set as an additional variable that is kept in the whole domain, together with the concentration parameter c . In order to keep the variables synchronized, an approach similar to the conservative strategy presented in [28] is conceivable.

Acknowledgments

The authors acknowledge discussions with Gustav Amberg, Minh Do-Quang, and Petia Boyanova on various aspects of phase field models. Computations were performed on resources provided by SNIC through Uppsala Multidisciplinary Center for Advanced Computational Science (UPPMAX) under Project p2010002. The first author was supported by the Graduate School in Mathematics and Computing (FMB).

References

- [1] S. Aland and A. Voigt. Benchmark computations of diffuse interface models for two-dimensional bubble dynamics. *Int. J. Numer. Meth. Fluids*, to appear, 2011.
- [2] D. M. Anderson, G. B. McFadden, and A. A. Wheeler. Diffuse-interface methods in fluid mechanics. *Annu. Rev. Fluid Mech.*, 30:139–165, 1998.

- [3] W. Bangerth, R. Hartmann, and G. Kanschat. deal.II — a general purpose object oriented finite element library. *ACM Trans. Math. Softw.*, 33(4):article no. 24, 2007.
- [4] W. Bangerth and G. Kanschat. *deal.II Differential Equations Analysis Library, Technical Reference*. <http://www.dealii.org>.
- [5] M. Benzi, G. H. Golub, and J. Liesen. Numerical solution of saddle point problems. *Acta Numerica*, 14:1–137, 2005.
- [6] P. Boyanova, M. Do-Quang, and M. Neytcheva. Efficient preconditioners for large scale binary Cahn–Hilliard models. *Comput. Meth. Appl. Math.*, to appear, 2011.
- [7] F. Boyer. A theoretical and numerical model for the study of incompressible mixture flows. *Comput. & Fluids*, 31:41–68, 2002.
- [8] J. U. Brackbill, D. B. Kothe, and C. Zemach. A continuum method for modeling surface tension. *J. Comput. Phys.*, 100:335–354, 1992.
- [9] J. W. Cahn and J. E. Hilliard. Free energy of a nonuniform system. I. Interfacial free energy. *J. Chem. Phys.*, 28(2):258–267, 1958.
- [10] A. Carlson, M. Do-Quang, and G. Amberg. Modeling of dynamic wetting far from equilibrium. *Phys. Fluids*, 21:121701, 2009.
- [11] S. H. Davis. Interfacial fluid dynamics. In G. K. Batchelor, H. K. Moffatt, and M. G. Worster, editors, *Perspectives in Fluid Dynamics*, pages 1–52. Cambridge University Press, Cambridge, 2002.
- [12] E. B. Dussan V. The moving contact line: The slip boundary condition. *J. Fluid Mech.*, 77(04):665–684, 1976.
- [13] D. A. Edwards, H. Brenner, and D. T. Wasan. *Interfacial Transport Processes and Rheology*. Butterworth–Heinemann, Stoneham, 1991.
- [14] H. Elman, D. Silvester, and A. Wathen. *Finite Elements and Fast Iterative Solvers with Applications in Incompressible Fluid Dynamics*. Oxford Science Publications, Oxford, 2005.
- [15] H. Emmerich. *The Diffuse Interface Approach in Materials Science: Thermodynamic Concepts and Applications of Phase-Field Models*. Springer, Berlin, 2003.
- [16] D. J. Eyre. An unconditionally stable one-step scheme for gradient systems, June 1998, unpublished.
- [17] J. P. d. S. R. Gago, D. W. Kelly, O. C. Zienkiewicz, and I. Babuška. A posteriori error analysis and adaptive processes in the finite element method: Part II — Adaptive mesh refinement. *Int. J. Num. Meth. Engrg.*, 19:1621–1656, 1983.
- [18] C. Galusinski and P. Vigneaux. On stability condition for bifluid flows with surface tension: Application to microfluidics. *J. Comput. Phys.*, 227:6140–6164, 2008.
- [19] M. W. Gee, C. M. Siefert, J. J. Hu, R. S. Tuminaro, and M. G. Sala. ML 5.0 Smoothed Aggregation User’s Guide. Technical Report 2006-2649, Sandia National Laboratories, 2006.
- [20] M. Germano. Properties of the hybrid RANS/LES filter. *Theoret. Comput. Fluid Dynamics*, 17:225–231, 2004.
- [21] E. Hairer, S. P. Nørsett, and G. Wanner. *Solving Ordinary Differential Equations I. Non-stiff Problems*. Springer Verlag, Berlin, 2nd edition, 1993.
- [22] D. Hartmann, M. Meinke, and W. Schröder. The constrained reinitialization equation for level set methods. *J. Comput. Phys.*, 229:1514–1535, 2010.
- [23] L. M. Hocking. A moving fluid interface. Part 2. The removal of the force singularity by a slip flow. *J. Fluid Mech.*, 79(2):209–229, 1977.
- [24] C. Huh and L. E. Scriven. Hydrodynamic model of steady movement of a solid/liquid/fluid contact line. *J. Colloid Interf. Sci.*, 35(1):85–101, 1971.
- [25] S. Hysing, S. Turek, D. Kuzmin, N. Parolini, E. Burman, S. Ganesan, and L. Tobiska.

- Quantitative benchmark computations of two-dimensional bubble dynamics. *Int. J. Numer. Meth. Fluids*, 60:1259–1288, 2009.
- [26] D. Jacqmin. Calculation of two-phase Navier–Stokes flows using phase-field modeling. *J. Comput. Phys.*, 155(1):96–127, 1999.
- [27] D. Jacqmin. Contact-line dynamics of a diffuse fluid interface. *J. Fluid Mech.*, 402:57–88, 2000.
- [28] C. E. Kees, I. Akkerman, M. W. Farthing, and Y. Bazilevs. A conservative level set method suitable for variable-order approximations and unstructured meshes. *J. Comput. Phys.*, 230:4536–4558, 2011.
- [29] J. Kim. A continuous surface tension force formulation for diffuse-interface models. *J. Comput. Phys.*, 204:784–804, 2005.
- [30] M. Kronbichler and K. Kormann. A generic interface for parallel cell-based finite element operator application. Submitted, 2011.
- [31] M. Kronbichler and G. Kreiss. A hybrid level–set–Cahn–Hilliard model for two-phase flow. In *Proceedings of the 1st European Conference on Microfluidics*, Bologna, Italy, 2008.
- [32] M. Kronbichler, C. Walker, G. Kreiss, and B. Müller. Multiscale modeling of capillary-driven contact line dynamics. Submitted, 2011.
- [33] J. Lowengrub and L. Truskinovsky. Quasi-incompressible Cahn–Hilliard fluids and topological transitions. *Proc. R. Soc. Lond. A*, 454:2617–2654, 1998.
- [34] K.-A. Mardal and R. Winther. Uniform preconditioners for the time dependent Stokes problem. *Numer. Math.*, 38:305–327, 2004.
- [35] A. Mazouchi, C. M. Gramlich, and G. M. Homsy. Time-dependent free surface Stokes flow with a moving contact line. I. Flow over plane surfaces. *Phys. Fluids*, 16(5):1647–1659, 2004.
- [36] A. Novick-Cohen. The Cahn–Hilliard equation. In C. M. Dafermos and E. Feireisl, editors, *Handbook of Differential Equations: Evolutionary Equations*, volume 4, pages 201–228. Elsevier, 2008.
- [37] E. Olsson and G. Kreiss. A conservative level set method for two phase flow. *J. Comput. Phys.*, 210:225–246, 2005.
- [38] E. Olsson, G. Kreiss, and S. Zahedi. A conservative level set method for two phase flow II. *J. Comput. Phys.*, 225:785–807, 2007.
- [39] S. Osher and R. P. Fedkiw. *Level Set Methods and Dynamic Implicit Surfaces*. Applied Mathematical Sciences. Springer, New York, 2003.
- [40] S. Osher and J. A. Sethian. Fronts propagating with curvature-dependent speed: Algorithms based on Hamilton–Jacobi formulations. *J. Comput. Phys.*, 79(1):12–49, 1988.
- [41] T. Qian, X.-P. Wang, and P. Sheng. Molecular hydrodynamics of the moving contact line in two-phase immiscible flows. *Comm. Comput. Phys.*, 1(1):1–52, 2006.
- [42] A. Quarteroni and A. Valli. *Numerical Approximation of Partial Differential Equations*. Springer Series in Computational Mathematics. Springer, Berlin, 1994.
- [43] W. Ren and W. E. Boundary conditions for the moving contact line problem. *Phys. Fluids*, 19:022101, 2007.
- [44] W. Ren, D. Hu, and W. E. Continuum model for the moving contact line problem. *Phys. Fluids*, 22:102103, 2010.
- [45] M. Renardy, Y. Renardy, and J. Li. Numerical simulation of moving contact line problems using a volume-of-fluid method. *J. Comput. Phys.*, 171(1):243–263, 2001.
- [46] Y. Saad. *Iterative Methods for Sparse Linear Systems*. SIAM, Philadelphia, second edition, 2003.
- [47] J. A. Sethian. *Level Set Methods and Fast Marching Methods. Evolving Interfaces in*

Computational Geometry, Fluid Mechanics, Computer Vision, and Materials Science. Cambridge University Press, 2000.

- [48] I. Singer-Loginova and H. M. Singer. The phase field technique for modeling multiphase materials. *Rep. Prog. Phys.*, 71:106501, 2008.
- [49] P. D. M. Spelt. A level-set approach for simulations of flows with multiple moving contact lines with hysteresis. *J. Comput. Phys.*, 207:389–404, 2005.
- [50] M. Sussman and E. Fatemi. An efficient, interface-preserving level set redistancing algorithm and its application to interfacial incompressible fluid flow. *SIAM J. Sci. Comput.*, 20(4):1165–1191, 1999.
- [51] M. Sussman, P. Smereka, and S. Osher. A level set method for computing solutions to incompressible two-phase flow. *J. Comput. Phys.*, 114(1):146–159, 1994.
- [52] J. D. van der Waals. The thermodynamic theory of capillarity under the hypothesis of continuous variation of density. *J. Stat. Phys.*, 20(2):200–244, 1979. Originally published in Dutch “Thermodynamische theorie der capillariteit in de onderstelling van continue dichtheidsverandering” in *Verhandel. Konink. Akad. Wet.* Amsterdam, 1893.
- [53] W. Villanueva and G. Amberg. Some generic capillary-driven flows. *Int. J. Multiphase Flow*, 32:1072–1086, 2006.
- [54] P. Yue, C. Zhou, and J. J. Feng. Sharp-interface limit of the Cahn–Hilliard model for moving contact lines. *J. Fluid Mech.*, 645:279–294, 2010.
- [55] S. Zahedi, K. Gustavsson, and G. Kreiss. A conservative level set method for contact line dynamics. *J. Comput. Phys.*, 228(17):6361–6375, 2009.
- [56] S. Zahedi, M. Kronbichler, and G. Kreiss. Spurious currents in finite element based level set methods for two-phase flow. *Int. J. Numer. Meth. Fluids*, to appear, 2011.